JOURNAL OF GEOPHYSICAL RESEARCH, VOL. 103, NO. A8, PAGES 17,215-17,222, AUGUST 1, 1998

Iron freeze-in temperatures measured by SOHO/CELIAS/CTOF

M. R. Aellig,[1] H. Grünwaldt,[2] P. Bochsler,[1] P. Wurz,[1] S. Hefti,[1]
R. Kallenbach,[1] F. M. Ipavich,[3] W. I. Axford,[2] H. Balsiger,[1] A. Bürgi,[4]
M. A. Coplan,[3] A. B. Galvin,[3] J. Geiss,[1] F. Gliem,[5] G. Gloeckler,[3]
M. Hilchenbach,[2] D. Hovestadt,[4] K. C. Hsieh,[6] B. Klecker,[4] M. A. Lee,[7]
S. Livi,[2] G. G. Managadze,[8] E. Marsch,[2] E. Möbius,[7] M. Neugebauer,[9]
K.-U. Reiche,[5] M. Scholer,[4] M. I. Verigin,[8] and B. Wilken[2]

Abstract. The CELIAS particle experiment on SOHO contains the Charge Time Of Flight (CTOF) mass spectrometer which measures the ionic and elemental composition of minor ions in the solar wind. In this paper we present iron freeze-in temperatures derived with a time resolution of 5 min. They indicate that some of the filamentary structures of the inner corona observed in Hα survive in the interplanetary medium as far as 1 AU.

1. Introduction

The CELIAS/CTOF time-of-flight (TOF) mass spectrometer [*Hovestadt et al.,* 1995] on board the SOHO mission measures the elemental and ionic composition of the minor ions in the solar wind. On their way from the solar surface through the corona into the interplanetary medium, minor ions become highly ionized by collisions with hot electrons. Because of the decreasing electron density with increasing distance from the solar surface and the decreasing charge exchange rates with decreasing electron temperature, the charge state distributions eventually freeze and remain unaltered throughout their further travel through the heliosphere. Therefore charge spectra measured at 1 AU serve as a valuable diagnostic tool for temperature and density variations in the inner corona [e.g., *Owocki et al.,* 1983]. Coronal temperatures are inferred from density ratios of adjacent charge states. The freeze-in temperature derived from a given density ratio is the electron temperature that reproduces this ratio in a static situation. For the analyzed iron charge states we use the ionization and recombination rates of *Arnaud and Raymond* [1992].

Measurements of the iron charge state distributions have been performed, e.g., with ICI on ISEE 3 using one freeze-in temperature to describe the charge states of iron in the range from Fe^{10+} to Fe^{13+} [*Schmid et al.,* 1988], and with Ulysses/SWICS, both, in and out of the ecliptic [e.g., *Geiss et al.,* 1992; *Galvin et al.,* 1995; *Geiss et al.,* 1995; *Ko et al.,* 1996]. Because of the high geometric factor of the CTOF sensor and the threeaxis stabilization of the SOHO spacecraft, which allows an uninterrupted view of the Sun, sensitivity and duty cycle are significantly increased compared to earlier experiments and result in a considerably improved time resolution.

In the next section we present freeze-in temperatures for different adjacent iron charge states which are derived from the so-called matrix elements of CTOF with high time resolution. Structures observed in the freeze-in temperatures as well as their absolute values are discussed. In Appendix A we describe the data products received from the CTOF sensor and illustrate them with flight data with special emphasis on the iron ions. In Appendix B the data analysis and elements of the instrument response model are presented.

2. Results

The procedure outlined in Appendix B was applied to CTOF data to calculate the freeze-in temperature of the ion pairs Fe^{9+}/Fe^{8+}, Fe^{10+}/Fe^{9+}, Fe^{11+}/Fe^{10+}, and Fe^{12+}/Fe^{11+} from the density ratios of the corresponding charge states with the maximum time resolution of

---

[1] Physikalisches Institut, University of Bern, Bern, Switzerland.

[2] Max-Planck-Institut für Aeronomie, Lindau, Germany.

[3] Department of Physics and Astronomy and IPST, University of Maryland, College Park.

[4] Max-Planck-Institut für extraterrestrische Physik, Garching, Germany.

[5] Institut für Datenverarbeitung, Technische Universität, Braunschweig, Germany.

[6] Department of Physics, University of Arizona, Tucson.

[7] Institute for the Study of Earth, Oceans, and Space, University of New Hampshire, Durham.

[8] Institute for Space Physics, Moscow, Russia.

[9] Jet Propulsion Laboratory, Pasadena, California.

Paper number 98JA00588.
0148-0227/98/98JA-00588$09.00

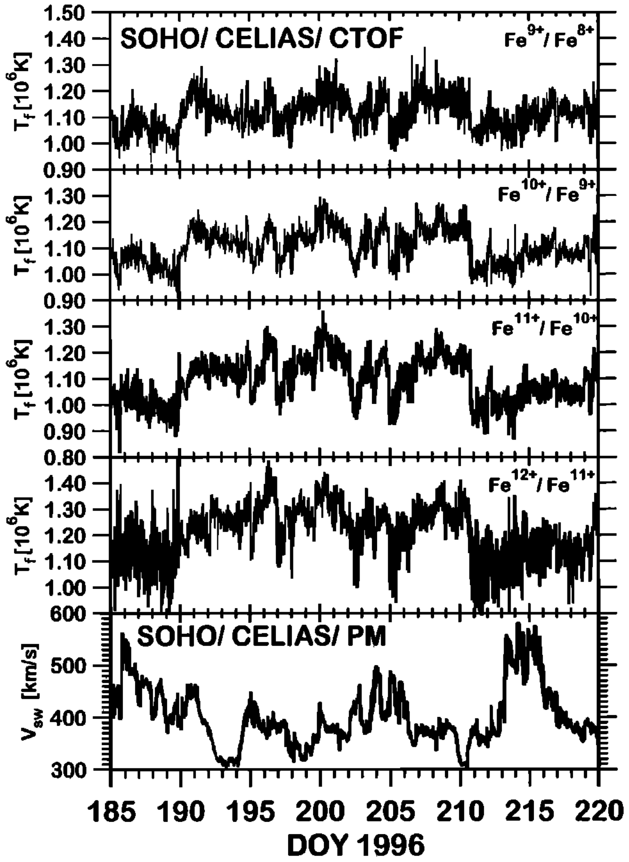

Figure 1. Coronal freeze-in temperatures for four pairs of iron charge states. The temperatures are determined with the maximum time resolution of five minutes and smoothed with a boxcar average 25 min wide. In the lowest panel the proton speed is displayed. Because of the high sensitivity of CTOF we detect short-scaled features in the freeze-in temperatures indicating small-scale variations of the electron density and temperature in the freeze-in region at a few solar radii.

5 min for an extended period of 35 days in which the solar wind bulk velocity was ranging between 300 and less than 600 km/s. The resulting temperatures have been smoothed with a boxcar average of 25 minutes width. The four freeze-in temperatures displayed in Figure 1 show very similar temporal evolutions with considerable variations on short timescales of a few hours (e.g., at the beginning of DOY 212). The common behavior on short time scales is also seen in the steep decrease of T_f occurring at the end of DOY 210. In Figure 2 this decrease as well as some other short-scaled features are displayed in detail. Such features can be used to distinguish between temporal and spatial effects as is shown by the following argument. Consider as an example the increase of T_f which was observed during the first 7 hours of DOY 212. Assuming that such a feature is produced by dispersion of a very short pulse of increased T_f, generated in the solar wind near the freeze-in point, it is possible to derive an upper limit of the thermal speed of iron ions which could cause the dispersion. From the observed width we obtain a dispersion speed of 5 km/s which is much less than the thermal speed of iron of 20 km/s observed at 1 AU for this time period. Thus we discard a purely temporal change of conditions as the origin of this feature. We rather ascribe this increase to the distinct conditions in a laterally confined flux tube which extends into the interplanetary medium. Consequently, the duration of this peak of 7 hours translates to a width of the flux tube on the solar surface of a few 10^4 km, assuming radial expansion.

Though the slow solar wind is known to vary stronger and faster in its bulk properties than the fast solar wind emerging from coronal holes, our observations suggest that the acceleration process of the slow solar wind conserves also small-scale variations in the coronal source region conditions as far as 1 AU. Such filamentary structures in the corona are observed, e.g., in Hα [*Koutchmy,*

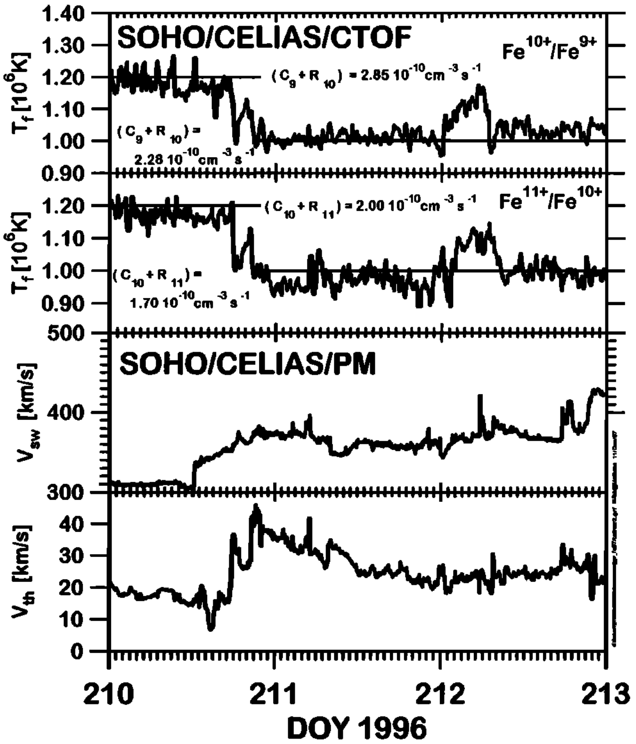

Figure 2. Coronal freeze-in temperatures for two pairs of iron charge states are shown in greater detail. Both the steep gradient on DOY 210 and the sharp peak on DOY 212 are displayed here. The latter does not seem to be related to any notable change in the proton kinetic parameters. The width of the peak of approximately 7 hours translates to a structure size on the Sun of a few 10^4 km. Prior to DOY 210.8 both freeze-in temperatures have about the same values but after the drop $T_{11/10}$ is lower than $T_{10/9}$. From the sum of the rate coefficients, given for two electron temperatures (1.0×10^6 K, 1.2×10^6 K), $T_{11/10}$ is expected to be higher because it freezes closer to the Sun. C_i denotes the ionization rate of Fe^{i+}, and R_i the recombination rate of Fe^{i+}.

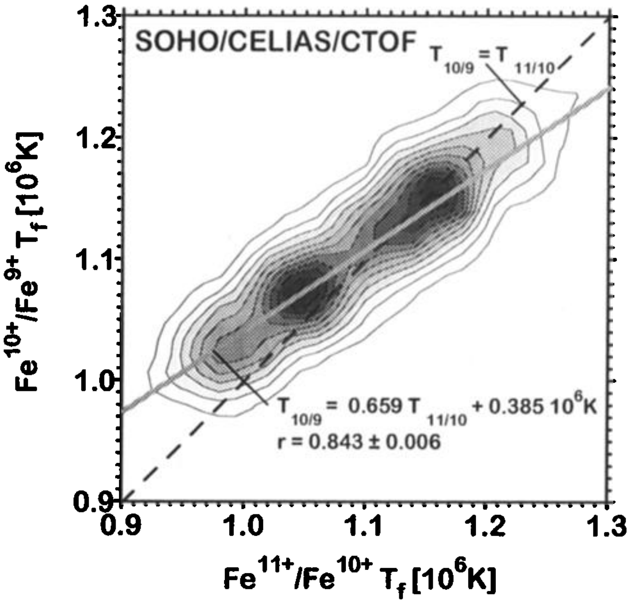

Figure 3. Correlation of the freeze-in temperatures derived from the pairs Fe^{10+}/Fe^{9+} and Fe^{11+}/Fe^{10+}. The temperatures have been smoothed with a boxcar average of 25 min width. Typical statistical uncertainties are of the order of 4×10^4 K for both temperatures. The linear correlation coefficient r is 0.84. It is shown in Appendix B that the temperature determination is anticorrelated. For low temperatures, $T_{10/9}$ is generally higher than $T_{11/10}$, while at higher temperatures, $T_{10/9}$ is approximately equal to $T_{11/10}$ or even below $T_{11/10}$.

1977]. The study of small scale structures traced by minor ions in the solar wind in such detail is, to our knowledge, for the first time possible with data from the CTOF sensor since its active area is larger and its duty cycle is higher than those of previous instruments.

Figure 3 displays the good correlation between the freeze-in temperatures $T_{10/9}$ derived from the ion pair Fe^{10+}/Fe^{9+} and $T_{11/10}$ derived from the ion pair Fe^{11+}/Fe^{10+} for the whole period analyzed. Though the temperature determinations are intrinsically anticorrelated (see Appendix B) the linear correlation coefficient amounts to 0.84. Typical uncertainties are 0.04×10^6 K for both temperature estimates.

From the whole period of 35 days the mean persistence time of the iron freeze-in temperatures determined was calculated from exponential fits to the short-term autocorrelation functions of the different temperatures to be 12 hours. This is consistent with the persistence time of the freeze-in temperature of O^{7+}/O^{6+} reported by *Bochsler et al.* [1997], but there are strong indications of nonstationarity (S. Hefti et al., manuscript in preparation, 1998).

The mean freeze-in temperatures calculated for the time period shown in Figure 1 are given in Table 1. Also, in Table 1 the freeze-in temperatures derived from the charge state spectra integrated over the whole period are given. We see that the two methods yield different values for the freeze-in temperatures. This demonstrates the necessity for high time resolution at least in the variable slow solar wind. From the integrated charge spectrum we derive decreasing temperatures with decreasing charge numbers, whereas the mean values of the temperatures derived with 5-min time resolution do not show this trend.

Since the recombination and ionization rates are not the same for every pair of charge states, freezing is expected to occur at different electron densities. Because higher charge states have lower rate coefficients at a given electron temperature, they are expected to freeze at higher electron densities and, because iron is known to freeze well beyond the coronal temperature maximum, also at higher electron temperature. Thus freeze-in temperatures derived from iron ions with higher charges should be higher. However, the averaged temperatures contradict this picture and imply a positive electron temperature gradient even at distances of a few solar radii from the solar surface whereas the temperatures drawn from the averaged charge spectrum do not show such an intriguing result. Possible uncertainties of the rate coefficients will not account for this implausible positive temperature gradient as long as the higher charged ions have lower rate coefficients. However, the presence of suprathermal electrons not considered in the above discussion might alter the rate coefficients sufficiently to explain the observations.

The results of Ulysses/SWICS data derived by *Galvin et al.* [1995] and by *Geiss et al.* [1995] imply that $T_{11/10}$ is lower than $T_{10/9}$ in the coronal hole type solar wind. This also disagrees with the simple picture of negative density and temperature gradient. Based on a 100 day average of polar coronal hole type solar wind, *Ko et al.* [1996] derived freeze-in temperatures for different species including iron, and indicate that $T_{11/10}$ is higher than $T_{10/9}$. The iron freeze-in temperatures observed in the slow solar wind ($v_p < 600$ km/s) based on CELIAS/CTOF measurements are consistent with the corresponding relative ionic abundances of low charged iron ions in the slow solar wind derived by *Geiss et al.* [1992] based on Ulysses/SWICS data. The iron freeze-in temperatures derived from CTOF data are, however, lower than the values derived from SWICS in the coronal hole associated solar wind, though the maximum electron temperature in the polar coronal holes is known to be lower than in the equatorial regions.

Table 1. Mean Freeze-in Temperatures

Ion Pair	$\overline{T_f}$	T_f From Mean Charge Distribution
Fe^{9+}/Fe^{8+}	1.11×10^6 K	1.11×10^6 K
Fe^{10+}/Fe^{9+}	1.10×10^6 K	1.12×10^6 K
Fe^{11+}/Fe^{10+}	1.09×10^6 K	1.13×10^6 K
Fe^{12+}/Fe^{11+}	1.19×10^6 K	1.26×10^6 K

This reflects the fact that in the polar coronal holes a given ion pair freezes closer to the Sun due to the lower electron density and/or the faster outflow of the ions. While the lower electron density leads to an increase of the charge modification time, the fast outflow speed shortens the expansion time of the solar wind.

The fact that $T_{10/9}$ is generally higher than $T_{11/10}$ in the slow solar wind is also seen from Figure 3. At lower $T_{11/10}$ this is most pronounced whereas at higher $T_{11/10}$ the difference is getting smaller. In Figure 2 the same observation is seen in an example of a fast transition from high freeze-in temperatures to low freeze-in temperatures. Prior to the steep decrease on DOY 210.8 both freeze-in temperatures have about the same value. After the drop, $T_{11/10}$ is lower than $T_{10/9}$ though from the corresponding rate coefficients it is expected to be higher for the lower as well as for the higher temperature. A more detailed analysis will show how far these observations could be reconciled with plausible electron temperature profiles in the inner corona once the impact of suprathermal electrons is better understood.

3. Conclusions

First iron charge state spectra obtained from SOHO/CELIAS/CTOF illustrate the excellent time resolution that is achieved in determining coronal electron temperatures with this sensor. The rapid and consistent changes in the freeze-in temperature calculated from four pairs of iron charge states confirm the patchy structure of the corona with length scales of some 10^4 km and reveal the survival of these structures from a few solar radii throughout 1 AU.

Appendix A: On-Board Classification and Data Products

The classification of CTOF data in the digital processing unit (DPU) approximates the mass per charge of a detected particle

$$M/Q = f(\tau, E/Q) \qquad \text{(A1)}$$

using a polynomial expansion with a total of nine coefficients. The TOF is denoted by τ and E/Q is the energy per charge of the particle when entering the instrument. The approximation of the mass of a particle

$$M = g(\tau, E_{ssd}) \qquad \text{(A2)}$$

uses a polynomial expansion with six coefficients. These numerical approximations include the energy loss in the carbon foil and the nuclear defect in the solid state detector, respectively. The 15 coefficients have been implemented according to the results of the final flight model calibration.

The major block of telemetry data contains the spectral information in the form of (1) pulse height raw data (E/Q, τ, and E_{ssd}), (2) spectral matrix rates (SMR), and (3) matrix elements (ME). These three types of data products are described and illustrated in the following subsections. While only a fraction of events is transmitted as pulse height data, all events detected are contained in the SMR and ME.

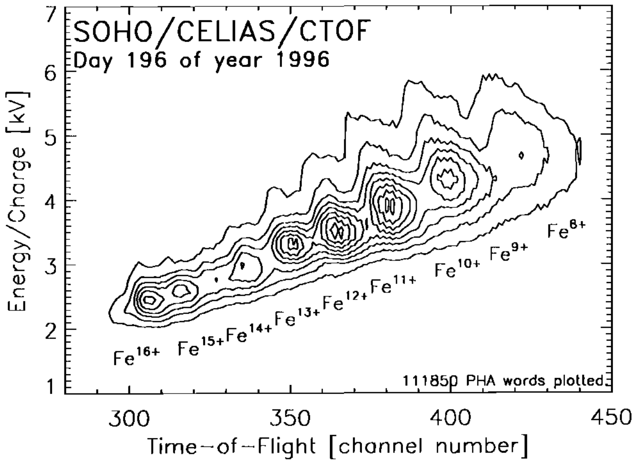

Figure A1. Histogram of TOF τ and energy per charge E/Q derived from pulse height data of day 196 of 1996. The contour levels are linearly spaced. The energy measured with the solid state detector is not shown, but was used to discriminate sulfur and silicon against iron. There are atypical high amounts of highly charged iron ions such as Fe^{16+} and Fe^{15+} observed in this period, which is explained by rather high electron temperatures in the coronal source region.

A.1. Pulse Height Data

The pulse height data consist of the TOF τ, the energy measured by the solid state detector E_{ssd}, and the E/Q step, at which the ion was registered. Because of the large effective area of the sensor of 16 mm^2 and the limited telemetry rate, not all pulse height analysis (PHA) words can be transmitted. Nevertheless, PHA raw data are indispensable for careful data analysis and in-flight calibration. In Figure A1, some of the accumulated PHA words of day 196 in 1996 are shown. The large amount of approximately 112,000 PHA words accumulated from iron ions during 1 day of operation in the solar wind reflects the high sensitivity of the sensor. The charge state peaks are well separated and can easily be identified. The abscissa indicates the measured TOF and the ordinate is the value of E/Q. The width of the peaks along the TOF axis reflects the energy straggling in the carbon foil, which leads to a variation in the TOF. The angular scattering in the carbon foil and at the grids in the TOF section leads to an increase of the path length, which is less important for the width of the peaks along the TOF axis. Because of the thermal velocity distribution of the solar wind ions and the bulk velocity variations during the period of accumulation, the individual peaks are also spread along the E/Q axis. Despite this spreading the identification of the iron species is simple since iron is much heavier than the equally abundant silicon and sulfur which only interfere at lower M/Q values. Atypical for the quiet solar wind are large amounts of highly ionized iron ions such as Fe^{16+} and Fe^{15+}. Although the telemetry restriction becomes more important at lower M/Q, the measured Fe^{16+} and Fe^{15+} fluxes are higher than the flux of Fe^{14+}.

A.2. Spectral Matrix Rates

The spectral matrix rates (SMR) contain 508 individual boxes in the $M - M/Q$ matrix of the PHA data. This matrix is a two-dimensional histogram in which events classified by the on-board processing of the primary quantities E/Q, τ, and E_{ssd} using (A1) and (A2) are accumulated. Each of these 508 boxes in the $M - M/Q$ table has a third dimension containing a reduced E/Q information from which the kinetic parameters are derived. The total size of the SMR is 508×21 entries, reducing the event space by more than 3 orders of magnitude compared to the PHA data.

A.3. Matrix Elements

The matrix elements (ME) consist of 1608 distinct boxes in the $M - M/Q$ table and have a higher resolution in mass and mass per charge than the SMR. However, the E/Q spectral information is lost in the ME because they are accumulated over a full cycle of E/Q stepping. Like the SMR the ME are transmitted once per sensor cycle, i.e., every 5 min. The densities of the individual iron charge states are derived from ME data.

Appendix B: Data Analysis

This section summarizes some key elements of the data analysis. First, we describe the general approach to the data analysis and then present some elements of the instrument response model. By the determination of the freeze-in temperatures based on data from one instrument cycle of 5 min duration we demonstrate the high temporal resolution of the CTOF sensor.

B.1. Extracting the Iron Densities

To obtain the densities of the individual species we apply the forward modelling technique. Since we intend to use ME for the determination of densities, we construct an instrument response model for a given species k, denoted by $G_{ik}(v_{0k}, T_k, M_k, Q_k)$, that yields the expected number of counts in every ME i for unit density. The model response depends on the drift velocity v_{0k} of the species, the kinetic temperature T_k, the mass M_k, and the charge Q_k. The latter is used to calculate the total energy of the ion after the post-acceleration. Thus the model accounts for different detection efficiencies of different charge states of a given element. For K different species the model is represented by the system of equations:

$$\mu_i = G_{i1}\, n_1 + G_{i2}\, n_2 + \ldots + G_{iK}\, n_K \qquad \text{(B1)}$$

where μ_i denotes the expected number of counts in the ME i given the densities of the individual species by n_k. We assume Poisson statistics to hold, and thus we invert (B1) for the densities by maximizing the logarithm of the likelihood

$$\ln L = \sum_{i=1}^{l} d_i \ln(\mu_i) - \mu_i + \text{const} \qquad \text{(B2)}$$

where $\vec{d}$ denotes the counts measured in the l selected matrix elements. Given the solar wind kinetic properties, 250 matrix elements in the iron region in the $M - M/Q$ table were inverted to yield densities of the individual iron charge states from Fe^{7+} to Fe^{16+}. In this model the contributions from the neighboring silicon and sulfur ions are taken into account. However, these corrections are only relevant for the higher charge states of iron.

The forward model assumes equal flow and thermal velocities for all iron charge states. The flow velocity was set equal to the flow velocity of O^{6+} derived by *Hefti* [1997], and the thermal velocity of the iron ions is based on the thermal velocity of O^{6+} by assuming a mass-proportional temperature. It was found by inversion of synthetic spectra that deviations of the thermal velocity from the true value are not critical to the density estimate. If the flow speed deviates from the true value by a certain percentage, the deconvolved density

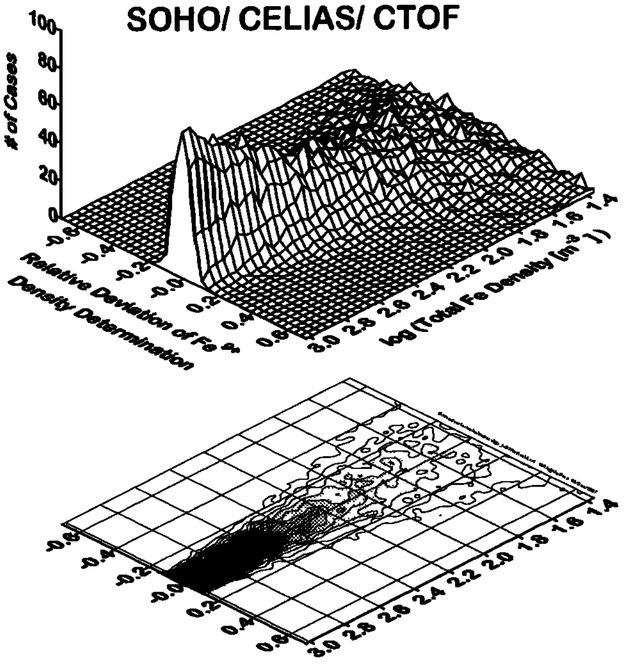

Figure B1. The performance of the inversion algorithm is illustrated with a histogram of the relative deviations of the density of Fe^{9+} from the true value. A total of 50,000 synthetic spectra were inverted. The charge state distribution was calculated from the total density assuming a single electron temperature ($T_e = 1.15 \times 10^6$ K).

was shown to deviate approximately by the same relative amount from its true value. Thus, if we assume equal velocities for two charge states which differ in speed by 1% the error in the density ratio of these two charge states is approximately 1%, which is below the typical statistical uncertainty of the density estimate in one cycle of 5 min. If the velocities are equal, then a deviation from the true velocity does not affect the resulting freeze-in temperatures, since they are calculated from ratios of densities.

The inversion algorithm was tested by the inversion of 50,000 synthetic spectra that were obtained from the forward model by application of a Poisson random number generator. Given the total density of iron we assumed one single electron temperature to derive the charge state distribution ($T_e = 1.15 \times 10^6$ K). For a grid of 50 values of total iron densities the relative deviations of the inverted density of Fe^{9+} were derived. The resulting histogram is shown in Figure B1. The relative uncertainty increases with decreasing total iron density, and we get an unbiased estimate for the Fe^{9+} density for a total iron density as low as approximately 25 m^{-3} if we know the kinetic parameters precisely. For the about equally abundant Fe^{10+} ion a similar result is obtained whereas the less prominent charge states are determined with larger uncertainties. To derive those densities a longer integration time is required to decrease the uncertainties. An example of the freeze-in temperature determination using 5 min of CTOF data is shown in section B.3.

B.2. Elements of the Instrument Response Model

For a Maxwellian distribution function of temperature T_k describing a solar wind species k of mass M_k, charge Q_k drifting radially away from the Sun with a speed v_{0k} we derived an approximate expression for the number of particles passing through the electrostatic analyzer at a given step j per unit time

$$\begin{aligned} c_{jk} \approx\; & n_k A \frac{v_{0k} + \frac{kT_{nk}}{\epsilon_v^2 v_{jk}}}{\left(1 + \frac{kT_{nk}}{\epsilon_v^2 v_{jk}^2}\right)^{3/2}} \\ & \times \left[\frac{v_{jk}}{v_{0k}} \frac{\left(v_{0k} + \frac{kT_{nk}}{\epsilon_v^2 v_{jk}}\right)}{\left(v_{jk} + \frac{kT_{nk}}{\epsilon_v^2 v_{jk}}\right)} - \frac{kT_{nk}}{4 v_{0k}^2 \sigma_\beta^2} \right] \\ & \times \exp\left(- \frac{(v_{0k} - v_{jk})^2}{2(kT_{nk} + v_{jk}^2 \epsilon_v^2)} \right) \\ & \times \left[2\Phi\left(\frac{\alpha_c}{\sqrt{\frac{kT_{nk}}{v_{jk} v_{0k}}}} \right) - 1 \right] \left[2\Phi\left(\frac{\beta_c}{\sigma_\beta} \right) - 1 \right]^{-1} \\ & \times \left[2\Phi\left(\frac{\beta_c}{\sqrt{\frac{kT_{nk}}{v_{jk} v_{0k}} + \sigma_\beta^2}} \right) - 1 \right] \end{aligned} \tag{B3}$$

Table B1. Entrance System Parameters for CELIAS/CTOF

Parameter	Calibrated Value
α_c	0.42 rad
β_c	0.42 rad
σ_β	0.23 rad
ϵ_v	0.0121
A[a]	16 mm^2

[a] *Hovestadt et al.* (1995) gave erroneously a value of 8 mm^2.

The density of this species is denoted by n_k and T_{nk} denotes the temperature per mass. The quantity $v_{jk}(M_k, Q_k)$ is the acceptance speed of the species k at step j, i.e., the speed at which the transmission through the entrance system reaches its maximum. Selecting particles with an energy per charge value of U_j at step j the acceptance speed equals

$$v_{jk} = \sqrt{\frac{2 Q_k U_j}{M_k}} \tag{B4}$$

The parameters α_c, β_c, σ_β, and ϵ_v describing the angular and speed acceptance of the entrance system as well as the active area A have been derived from ground calibration [*Hefti*, 1997] and are summarized in Table B1. In the limiting case of very low kinetic temperature the count rate c_{jk} equals approximately $N\, v_{0k}\, A$ for the appropriate step number j.

For both (A1) and (A2), the TOF response of the ions have to be known in order to model accurately the instrument response in the $M - M/Q$ domain. The TOF peaks are described in terms of position and width. These parameters are determined for four different charge states at different step numbers j for an extended period of time from in-flight PHA data. Representing the energy loss ΔE in the carbon foil by a linear function of the total energy E_{tot} prior to the carbon foil passage, the inverse TOF square is a linear function of E_{tot}

$$\frac{1}{\tau^2} = a\, Q \left(\frac{E}{Q} + U_{acc} \right) + b \tag{B5}$$

Additionally, the charge state assignment of iron ions is done by means of (B5). Depending upon the charge state assignment we get different values for the parameters a and b of the linear fit. Figure B2 displays the residuals from the corresponding linear model for three different charge state assignments. We conclude that the assignment chosen for the middle panel holds since it produces the smallest reduced χ^2. The assignments that differ by one elementary charge show strong systematic deviations from the linear model and produce also larger reduced χ^2 and are therefore ruled out. Furthermore, the highest charge state observed with the charge state assignment adopted for the smallest χ^2 is Fe^{16+}, whereas in the other cases it would correspond to Fe^{15+} and Fe^{17+}, respectively. Since Fe^{16+} ions have

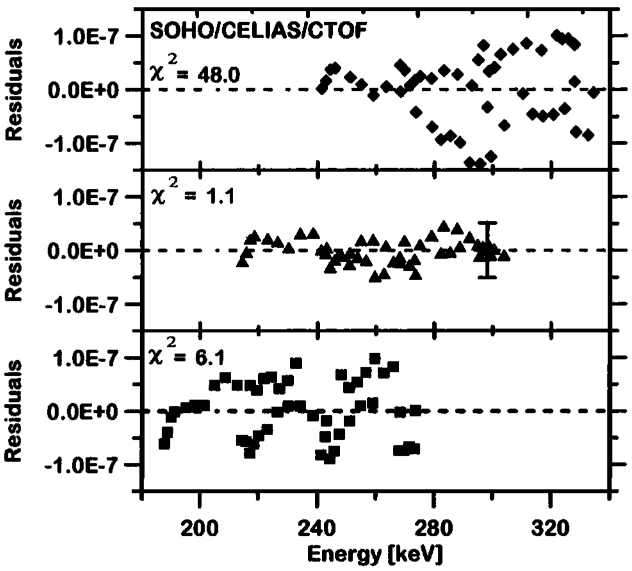

Figure B2. Deviations from the linear model used to describe the inverse TOF square as a function of the total energy before the carbon foil passage for three different charge state assignments. The charge assignment in the middle panel produces a reduced χ^2 of 1.1. If the actual charge assignment is shifted by one charge to (top) higher or (bottom) lower values, the residuals, and thus the reduced χ^2, increase considerably. Therefore these possibilities can be ruled out. A 2-σ error typical for all residuals is shown in the middle panel.

a noble gas electron configuration they are comparably stable to further ionization. This is another piece of evidence in favor of the chosen charge state assignment.

To get an accurate instrument response function G not only the positions of the peaks in TOF must be known for the appropriate energy range but also the peak shape must be determined. The solid state detector response in terms of peak positions and widths was also determined from in-flight PHA data. To get the instrument response in the $M-M/Q$ domain the response in terms of the primary measurements E/Q, τ, and E_{ssd} is subjected to the transformation equations (A1) and (A2). The transmission of the entrance system is given by (B3), and the absolute efficiency of the sensor is derived from prelaunch and postlaunch ground calibrations with the flight model and its spare model, respectively. The flight model has been calibrated with helium, nitrogen, and argon ions. With these species the mass range of solar wind ions is covered well, and extrapolations to the noncalibrated species can be done.

B.3. The Iron Freeze-in Temperature Determined With Highest Time Resolution

We derive freeze-in temperatures from the density ratio of adjacent iron charge states. The freeze-in temperatures of the ion pairs Fe^{10+}/Fe^{9+} and Fe^{9+}/Fe^{8+} were calculated from the density estimates based on 5 min of data. Numerical analysis of these data gives for $T_{9/8} =$

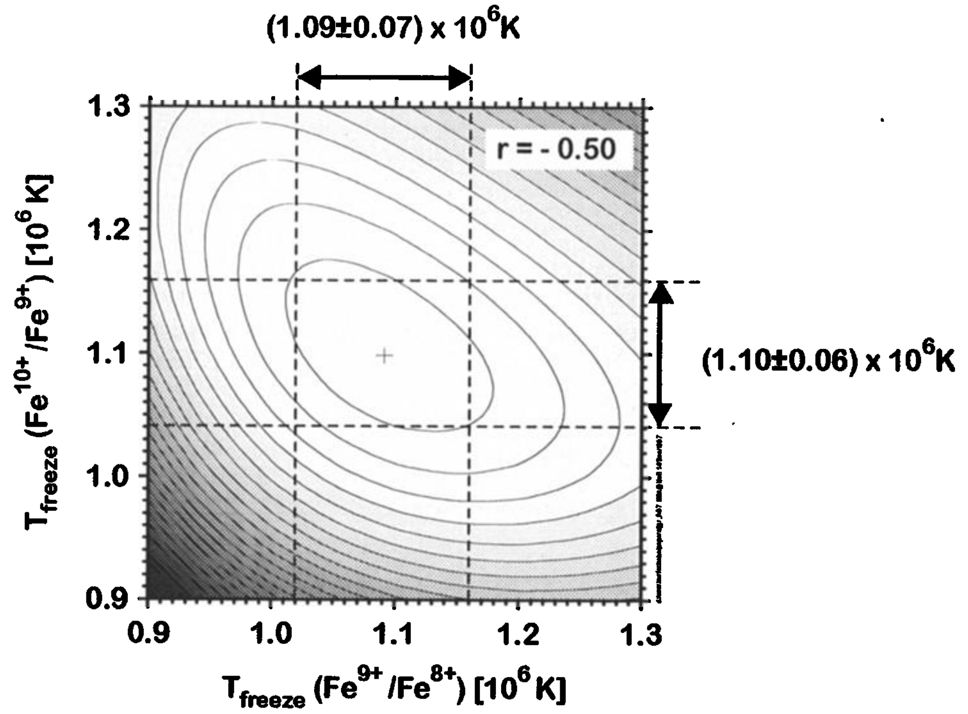

Figure B3. Contour plot of the natural logarithm of the likelihood. At the solution of the inversion problem, the likelihood takes on its maximum. The determination of the temperatures is anticorrelated, i.e., if one temperature is underestimated, the other is overestimated. For this temperature estimate, ME data of one instrument cycle (5 min) were used.

$(1.09\pm0.07)\times10^6 K$ and for $T_{10/9} = (1.10\pm0.06)\times10^6 K$. The estimates of the uncertainties of the freeze-in temperatures were derived from the covariance matrix of the densities, i.e., the inverted Hessian matrix, using the laws of error propagation. Similarly, the linear correlation coefficient between the two temperature determinations is calculated to be $r = -0.50$. That means that the two freeze-in temperatures cannot be independently determined.

In Figure B3 the natural logarithm of the likelihood is shown as a function of both freeze-in temperatures. The coordinates of the maximum of the likelihood give the solution of the inversion problem, and the curvature at the maximum is a measure for the statistical uncertainty. The sharper the maximum, the smaller is the uncertainty of the parameter estimate. For this calculation, the sum of the densities of Fe^{8+} to Fe^{10+} was set to the sum of their optimal estimations, and all other densities were individually set to their optimal values. The set of optimal densities n_k maximizes the likelihood given in (B2). The fact that $T_{9/8}$ and $T_{10/9}$ may not be determined independently is evident in Figure B3 from the tilt of the ridge relative to the coordinate axes. Note that this anticorrelation is only introduced by the inversion algorithm and by the resolution of the matrix elements. In a given matrix element, there may be contributions from two adjacent charge states. Thus, if the abundance of one charge state is overestimated, the other charge state is lowered. However, from a physical point of view one clearly expects the temperatures to correlate.

Acknowledgments. This work is supported by the Swiss National Science Foundation, by the PRODEX program of ESA, by DARA, Germany, under contracts 50 OC 89056 and 50 OC 96087, and by NASA, United States, under contract NAS-31166. CELIAS is a joint effort of 5 hardware institutions under the direction of MPE (prelaunch) and UBE (postlaunch). MPAe was the prime hardware institution for CTOF, UBE provided the deflection system, and TUB provided the DPU.

The Editor thanks Adam Szabo and Ernest Hildner for their assistance in evaluating this paper.

References

Aellig, M. R., Iron in the solar wind, Ph.D. thesis, Univ. of Bern, Bern, Switzerland, 1998.

Arnaud, M., and J. Raymond, Iron ionization and recombination rates and ionization equilibrium, *Astrophys. J.*, *398*, 394-406, 1992.

Bochsler, P., D. Hovestadt, H. Grünwaldt, M. Hilchenbach, F.M. Ipavich, M. R. Aellig, W. I. Axford, H. Balsiger, A. Bogdanov, A. Bürgi, M. A. Coplan, A. B. Galvin, J. Geiss, F. Gliem, G. Gloeckler, S. Hefti, K. C. Hsieh, D. L. Judge, R. Kallenbach, B. Klecker, H. Kucharek, S. E. Lasley, M. A. Lee, Y. Litvinenko, S. Livi, G. G. Managadze, E. Marsch, E. Möbius, M. Neugebauer, H. S. Ogawa, J. A. Paquette, K.-U. Reiche, M. Scholer, M. I. Verigin, B. Wilken, and P. Wurz, The Sun at minimum activity: Results from the CELIAS experiment on SOHO, *Eur. Space Agency Spec. Publ.*, *404*, 37-43, 1997.

Galvin, A. B., F. M. Ipavich, C. M. S. Cohen, G. Gloeckler, and R. von Steiger, Solar wind charge states measured by Ulysses/SWICS in the south polar hole, *Space Sci. Rev.*, *72*, 65-70, 1995.

Geiss, J., K. W. Ogilvie, R. von Steiger, U. Mall, G. Gloeckler, A. B. Galvin, F. M. Ipavich, B. Wilken, and F. Gliem, Ions with low charges in the solar wind as measured by SWICS on board Ulysses, in Proc. *Solar Wind Seven*, edited by E. Marsch and R. Schwenn, pp. 341-348, Pergamon, Tarrytown, N.Y., 1992.

Geiss, J., G. Gloeckler, R. von Steiger, H. Balsiger, L. A. Fisk, A. B. Galvin, F. M. Ipavich, S. Livi, J. F. McKenzie, K. W. Ogilvie, and B. Wilken, The southern high-speed stream: results from the SWICS instrument on Ulysses, *Science*, *268*, 1033-1036, 1995.

Hefti, S., Solar wind freeze-in temperatures and fluxes measured with SOHO/CELIAS/CTOF and calibration of the CELIAS sensors, Ph.D. thesis, Univ. of Bern, Bern, Switzerland, 1997.

Hovestadt, D., M. Hilchenbach, A. Bürgi, B. Klecker, P. Laeverenz, M. Scholer, H. Grünwaldt, W. I. Axford, S. Livi, E. Marsch, B. Wilken, H. P. Winterhoff, F. M. Ipavich, P. Bedini, M. A. Coplan, A. B. Galvin, G. Gloeckler, P. Bochsler, H. Balsiger, J. Fischer, J. Geiss, R. Kallenbach, P. Wurz, K.-U. Reiche, F. Gliem, D. L. Judge, H. S. Ogawa, K. C. Hsieh, E. Möbius, M. A. Lee, G. G. Managadze, M. I. Verigin, and M. Neugebauer, CELIAS - Charge, Element and Isotope Analysis System for SOHO, *Sol. Phys.*, *162*, 441-481, 1995.

Ko, Y.-K., L. A. Fisk, J. Geiss, G. Gloeckler, and M. Guhathakurta, An empirical study of the electron temperature and heavy ion velocities in the south polar coronal hole, *Sol. Phys.*, *171*, 345-361, 1997.

Koutchmy, S., Study of the June 30, 1973 transpolar coronal hole, *Sol. Phys.*, *51*, 399-407, 1977.

Owocki, S. P., T. E. Holzer, and A. J. Hundhausen, The solar wind ionization state as a coronal temperature diagnostic, *Astrophys. J.*, *275*, 354-366, 1983.

Schmid, J., P. Bochsler, and J. Geiss, Abundance of iron ions in the solar wind, *Astrophys. J.*, *329*, 956-966, 1988.

M. R. Aellig, H. Balsiger, P. Bochsler, J. Geiss, S. Hefti, R. Kallenbach, and P. Wurz, Physikalisches Institut, University of Bern, Sidlerstr. 5, CH-3012 Bern, Switzerland. (e-mail: maellig@soho.unibe.ch; hbalsiger@phim.unibe.ch; bochsler@soho.unibe.ch; geiss@issi.unibe.ch; hefti@soho.unibe.ch; kallenbach@issi.unibe.ch; wurz@soho.unibe.ch)

W. I. Axford, H. Grünwaldt, M. Hilchenbach, S. Livi, E. Marsch, and B. Wilken, Max-Planck-Institut für Aeronomie, D-37189 Lindau, Germany (e-mail: gruenwaldt @linax1.dnet.gwdg.de)

A. Bürgi, D. Hovestadt, B. Klecker, and M. Scholer, Max-Planck-Institut für extraterrestrische Physik, D-85740, Garching, Germany

M. A. Coplan, A. B. Galvin, G. Gloeckler, and F. M. Ipavich, Department of Physics and Astronomy and IPST, University of Maryland, College Park, MD 20742. (e-mail: ipavich@umdsp.dnet.nasa.gov)

F. Gliem and K.-U. Reiche, Institut für Datenverarbeitung, Technische Universität, D-38023 Braunschweig, Germany

K. C. Hsieh, Department of Physics, University of Arizona, Tucson, AZ 85721.

M. A. Lee and E. Möbius, Institute for the Study of Earth, Oceans, and Space, University of New Hampshire, Durham, NH 03824.

G. G. Managadze and M. I. Verigin, Institute for Space Physics, Moscow, Russia.

M. Neugebauer, Jet Propulsion Laboratory, Pasadena, CA 91103.

(Received March 25, 1997; revised December 16, 1997; accepted January 28, 1998.)